IEEE Open Journal of Antennas and Propagation

Received XX Month, XXXX; revised XX Month, XXXX; accepted XX Month, XXXX; Date of publication XX Month, XXXX; date of current version XX Month, XXXX.

Digital Object Identifier 10.1109/OJAP.2020.1234567

High-gain, Compact UWB Antenna for Wireless Power Transfer Based Wearable Applications

KARTHIK KAKARAPARTY, GRADUATE MEMBER, IEEE, AND IFANA MAHBUB*, SENIOR MEMBER, IEEE

[1]Department of Electrical and Computer Engineering, The University of Texas at Dallas,800 W Campbell Road,Richardson, Texas 75080

CORRESPONDING AUTHOR: IFANA MAHBUB, (e-mail: Ifana.Mahbub@utdallas.edu).

ABSTRACT The advancement of wearable ultra-wideband (UWB) antennas for wireless power transmission (WPT) requires a compact antenna design with high gain and wide bandwidth capability. A wearable UWB antenna is fabricated that is intended for wireless power transfer applications. A comparative analysis is presented with respect to the fabricated antenna's gain, bandwidth, and power transfer capability with the antenna in the air and when placed on the human skeletal muscle tissue phantom. The fabricated UWB antenna has a resonating frequency of 3.11 GHz. The designed UWB antenna has realized a gain of 6.35 dBi with fractional bandwidth (FBW) of 69.93%. The measured nearfield S_{21} parameter portrayed a maximum power transfer efficiency (PTE) efficiency of 66.3% for a 0.3λ transfer distance along with the estimated specific absorption rate (SAR) value of 0.794 W/kg when averaged over 10 g tissue and 1.02 W/kg when averaged over 1 g tissue portrays that the proposed design is safe and suitable for wearable applications.

INDEX TERMS Wearable antenna, High gain, Ultra-wideband (UWB), Flexible antenna, Human tissue phantom, Wireless power transfer (WPT), Phantom fabrication.

I. Introduction

AT the end of the 19th century, wireless energy transmission became a more and more intriguing research topic when Nikola Tesla made the discovery. [1]–[5]. In order to develop reliable wireless communication or WPT, the design approach of the antenna is a crucial part. An antenna with at least 0.5 GHz or with bandwidth more than 20% with respect to center frequency can be considered an ultra-wideband antenna (UWB) antenna. The creation of efficient ultra-wideband antennas is necessary owing to the rapid advancement of wireless technologies. Numerous sensors are now directly affixed to or even implanted within the human body [6]–[8]. With the use of wearable technology, practitioners can remotely monitor patients, diagnose illnesses, and treat patients remotely. The antenna must have good gain and relatively wide bandwidth while also being flexible, safe for the human body, and compact. Most literature studies indicate that microstrip patch antennas are suitable for these WPT applications due to their compact and inexpensive fabrication [9]–[18].

Recent prior works have contributed the design approaches for wearable and conformal antennas, but very few of those have focused on the antenna's ultra-wideband (UWB) operability, high gain, PTE enhancement, flexibility, and compactness [19]–[26]. Zhou et al. [19] introduced a compact broadband planar viaed double-spiral resonator, which significantly enhances the bandwidth (over 15%) while maintaining power transfer efficiency, addressing the inefficiencies commonly encountered in strongly coupled magnetic resonance (SCMR) systems due to high-dielectric

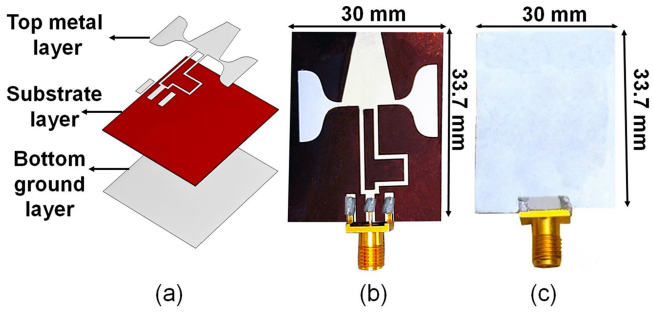

FIGURE 1. The proposed UWB antenna (a) Trimetric view portraying the individual design layers. The fabricated antenna (b) Front view (c) Back view.

This work is licensed under a Creative Commons Attribution 4.0 License. For more information, see https://creativecommons.org/licenses/by/4.0/

interference. This approach highlights the potential of design innovations in mitigating environmental factors that typically degrade performance. In another study, Hammoodi and Ali [20] investigated the bending effects on a UWB pentagonal antenna, confirming that its design maintains a robust bandwidth of 111.6% and consistent gain despite mechanical deformations, which is essential for wearable applications. Kanagasabai et al. [21] proposed a miniaturized circularly polarized antenna that leverages a textile substrate to achieve flexibility and integration with clothing, making it suitable for body-centric communications. This design further capitalizes on circular polarization's advantages, such as multipath immunity, to improve connectivity in wearable networks. Moreover, Gayen et al. [22] conducted a comprehensive review of planar miniaturized antennas for wireless capsule endoscopy, underscoring the need for optimization techniques and material compatibility in biomedical applications. Sharma et al. [23] presented a compact printed UWB monopole antenna with a high rejection capability across multiple bands, illustrating its potential for multifunctional wireless applications in space-constrained environments. Fadehan et al. [24] explored electromagnetic band gap (EBG) structures to achieve dual band-notch functionalities in UWB antennas, which could serve to avoid narrow-band interferences effectively. Lastly, Wagih et al. [25] developed a broadband, substrate-independent textile antenna capable of simultaneous near- and far-field wireless power transmission, demonstrating significant efficiency and compactness, thereby addressing both power harvesting and operational flexibility for wearable technologies. Collectively, these studies represent significant strides in advancing antenna technologies that cater to the multifaceted requirements of modern wearable applications.

Advancements in wearable antenna design have significantly improved the performance of antennas for Wireless body area networks (WBAN) applications. For example, Yimdjo Poffelie et al. introduced an all-textile ultra-wideband (UWB) antenna with a full-ground plane that minimizes backward radiation while ensuring high on-body fidelity, making it highly suitable for body-worn UWB communication systems [27]. Similarly, Samal et al. developed a textile-based multiband antenna using capacitive coupling techniques, which supports UWB and WLAN bands and performs robustly under on-body and bending conditions [28]. Furthermore, Chen et al. achieved substantial bandwidth improvements with a low-profile, circularly polarized patch antenna by employing Characteristic mode analysis (CMA), offering a compact and cost-effective solution with enhanced performance [29]. These contributions provide critical insights into addressing key challenges in wearable antenna systems, especially in terms of radiation performance, bandwidth enhancement, and flexibility.

Fernández et al. developed a 2.4 GHz fully woven textile-integrated circularly polarized antenna using a rectangular patch with chamfered corners and a T-match feeding network, achieving 45% efficiency under practical conditions and demonstrating excellent integration with textiles, though adapting this approach for diverse environmental conditions could unlock further potential [30]. Gopika et al. proposed a dual-port quasi-self-complementary antenna integrated with a Yagi element, achieving a 3 dB gain enhancement in the 1.8–2.3 GHz range and providing a compact and efficient solution for end-fire radiation, while future work could explore bandwidth enhancements for broader applicability [31]. Yang et al. achieved substantial bandwidth improvements of 120% by employing dispersive materials in wideband dielectric resonator antennas, ensuring stable radiation patterns for wireless power transfer systems, though exploring cost-effective production methods for these specialized materials could enhance practical adoption [32]. Ma et al. demonstrated a receiving antenna combining a magnetoelectric (ME) heterostructure and an inductive coil, enhancing magnetic field coupling at 54 kHz, which is highly effective for deeply implanted biomedical devices, while scaling the design for broader applications could further its impact [33]. Alemaryeen et al. optimized a 915 MHz implanted dipole antenna for biomedical applications, focusing on effective electromagnetic and thermal design to minimize tissue heating while maintaining efficient energy transfer, with opportunities to extend this approach to varied biological conditions for wider use [34].

The prior works presented the power transfer efficiency of the wearable antennas but did not show the specific absorption ratio (SAR) analysis averaged over 1 g and 10 g of tissue for the entire operational bandwidth of the antenna. Also, only a few prior works showed the performance of the antenna with and without the presence of the phantom, which is needed for more practical performance analysis. This paper extends the simulated model introduced in [6] by fabricating the antenna design and providing comprehensive measurement results, which are compared to the simulated data for validation. While the fundamental design remains consistent with [6], our work focuses on the practical implementation and performance evaluation of the antenna. The discussion on the fabrication process and testing methodologies has been expanded to highlight the innovation and practical relevance of the design.

Compared to traditional antenna designs, such as standard rectangular microstrip patches and bowtie antennas, the proposed antenna offers distinct advantages for wireless power transfer (WPT) applications through its wide bandwidth and compact form factor. The integration of a loop strip in the feed path significantly improves impedance matching and mitigates anti-phase currents, resulting in broader bandwidth coverage, which is crucial for efficient power transfer across a wide frequency range. Traditional microstrip patch antennas, while compact, typically exhibit limited bandwidth, and bowtie antennas, although offering wider bandwidth, often require larger physical sizes. In contrast, the proposed design maintains a compact size while achieving ultra-wideband

performance, making it highly suitable for WPT applications where both space efficiency and wide frequency coverage are critical.

The novelty of the work presented lies in its compact design with an incorporated loop strip within the feed structure that achieved wide operational bandwidth performance and high gain along with significant maximum PTE. This work bridges the gap to analyze the performance of the proposed antenna in the air and on a human phantom. The other contributions of this work are as follows: (1) Analysis of both near-field and far-field S_{21} parameters for PTE estimation, (2) Simulation for antenna structure deformation analysis, (3) Measured and simulated PTE analysis of antenna in air and on phantom cases, (4) SAR analysis over the operational bandwidth for both cases where SAR is averaged over 1 g and 10 g respectively, and (5) Estimation of power transfer efficiency of the proposed antenna when placed on a human skeletal tissue phantom both in near-field and far-field regions.

The remaining of the paper is structured as mentioned: Section II presents the antenna design methodology, and the human tissue phantom preparation procedure is discussed in Section A. Section B presents the fabrication procedure of the antenna. Section IV presents the antenna measurements and simulation procedures. In Section V, the measured and simulation results are discussed. Section VI comprises the concluding remarks and future works.

II. Antenna Design Methodology

The computer simulation technology (CST) suite is utilized in order to design the antenna. Polyimide with 0.1 mm thickness is the material of choice for the substrate of the proposed antenna due to its flexible and biocompatible nature. The polyimide substrate's tangent loss and dielectric constant are 0.0002 and 3.5, respectively. Silver (Ag) is selected as the patch and ground material. The proposed antenna has dimensions of $30 \times 33.7 \times 0.1004\ mm^3$. The trimetric view portraying the individual design layers is presented in Fig. 1(a), as depicted, an edge coaxial SMA feed technique is utilized to feed the antenna. The space between the SMA legs and the ground layer of the antenna is filled with a piece of styrofoam. The SMA legs are in contact with the ground layer via the solder paste. The other two SMA legs which are in contact with the top metal layer are responsible for bridging between the top and bottom layers. When such an antenna is placed on the phantom, the contact between both is established via the bottom ground layer. The front view of the fabricated antenna is depicted in Fig. 1(b), and the back view is presented in Fig. 1(c). The proposed antenna design is inspired by bow-tie antenna architecture, featuring flared elements that enhance gain by improving the aperture area for radiation. The optimized feed structure minimizes reflection losses and improves impedance matching, resulting in broader bandwidth. While the design underwent several iterations to refine key performance metrics, the final configuration emerged as an optimal solution, balancing size, bandwidth, and gain.

TABLE 1. The optimum antenna design variables

Variable	Value (mm)	Variable	Value (mm)
W_a	4.4	L_t	12.5
W_b	12	L_c	8.6
L_a	5.5	L_s	5.2
W_c	2	L	33.7
W	30	θ (in degrees)	60°

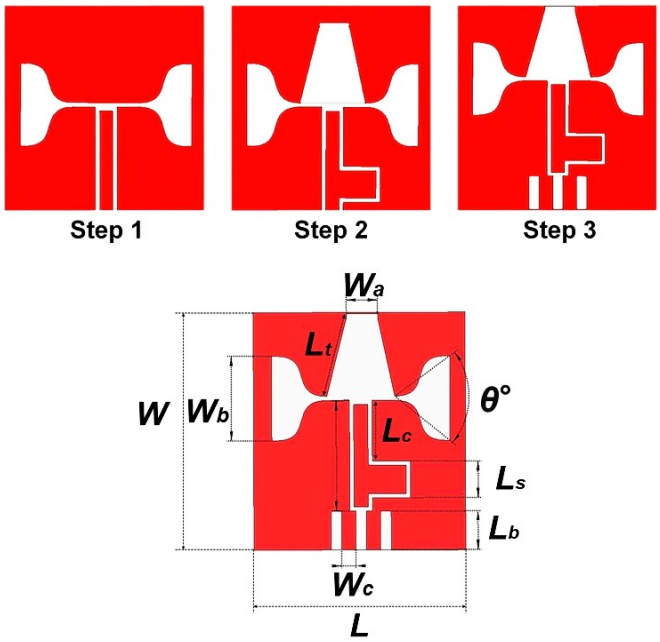

FIGURE 2. Design evolution of the proposed antenna, $1 \rightarrow 2 \rightarrow 3$, with final labeled version.

The design evolution of the proposed antenna is presented in Fig. 2. The waveguide edge port, which connects the top patch and ground, is utilized to feed the antenna structures for the initial 2 steps of design evolution. Step 3 incorporates the ground-source-ground (GSG) pads, which were edge-fed with a 50Ω matched port to test the S_{11} parameters. The proposed microstrip antenna design is inspired by a conventional bowtie antenna where its design is modified to smooth bell curve shapes identically on both the left and right sides. A trapezoidal structure has been added to the top to improve gain in radiation direction. The proposed antenna design includes a full ground plane at the bottom, which confirms that it is a microstrip antenna rather than a bowtie antenna. The full ground plane provides an effective ground reference that improves the radiation pattern and impedance matching of the antenna. The loop strip incorporated into the feed path of the antenna plays a key role in achieving ultra-wideband performance. It mitigates anti-phase mirror current issues that can impact the performance of the antenna, leading to improved bandwidth and stable performance of S_{11} and gain. Moreover, the use of the loop strip allows

TABLE 2. Material properties of phantom layers

Layer	Permittivity (ϵ_r)	Conductivity (S/m)	Density (kg/m^3)
Skin	36	5.01	1100
Fat	9.04	0.12	1100
Skeletal muscle	50	1.8	1060

for a more compact design, which is beneficial for practical applications. The antenna's ultra-wideband performance is achieved through careful design considerations and optimization of the loop-strip dimensions. The use of a full ground plane and loop strip in the antenna design ensures stable and efficient operation over a broad frequency range along with high gain across the operational band. The design variables and corresponding values are presented in Table I.

The proposed antenna outperforms a standard patch antenna by offering broader bandwidth, higher gain, and more compact size, while also being better suited for wearable applications. Unlike conventional patch antennas, which are typically limited in bandwidth, the proposed design achieves a fractional bandwidth of 69.93%, making it highly efficient for multi-frequency power transfer. Its compact dimensions allow for easy integration into space-constrained wearable devices without sacrificing performance. Additionally, the proposed antenna delivers a gain of 6.35 dBi, ensuring efficient power transfer even when placed on the human body, where standard rectangular microstrip antennas often experience performance degradation. The flexible and biocompatible nature of the antenna, along with its SAR compliance, ensures its suitability and safety for wearable applications.

III. Fabrication Procedure

A. Phantom preparation recipe

A simplified phantom recipe is utilized to replicate the average permittivity of human skeletal muscle tissue. A straightforward and uniform solution is created following the preparation guidelines outlined by the National Institute of Health (NIH) [35]. The recipe used for phantom fabrication comprises NaCl, oil, agar, benzoic acid (C_6H_5COOH), glycerine, and distilled water. A standard petri dish with a 96 mm diameter and 15 mm thickness is utilized as a container to hold the phantom mixture. As reported in [36], Gelatin, a thickening agent is used to solidify the prepared tissue-mimicking solution. The three layers considered for phantom simulation are chosen such that the average permittivity of the 3 layers (skin, fat, and human skeletal muscle) combined is nearly matched to the permittivity of the fabricated phantom. The fabricated phantom's permittivity is 30.6 and the average permittivity for 3 layers of the simulated phantom is 31.6. The aperture diameter of the phantom considered is 96 mm with an overall thickness of 15 mm. The material properties of the layers considered for the simulated model are presented in Table 2.

B. Antenna Fabrication Procedure

The proposed antenna is fabricated in the clean room utilizing the procedure involved in the Electron-beam physical vapor deposition (EBPVD) procedure, photo-lithography, and reactive-ion etching methodologies. The polyimide substrate is first coated with silver with a 200 nm thickness utilizing the Electron-beam physical vapor deposition (EBPVD) procedure. The EBPVD-based coated sample underwent a SU8-photoresist development procedure via a spin coating process. The sample then underwent UV light exposure by placing the fabricated photomask on top of it. The exposed oxide is then etched using reactive-ion etching, wherein the regions of the polyimide substrate's uppermost layer where there is no photoresist protection are removed. Then the sample is finally dipped into a photoresist stripper solution to remove the remaining photoresist.

IV. Antenna measurement and simulation

The proposed antenna's radiative near-field (RNF) and far-field (FF) regions are estimated using (1) and (2). As the antenna is placed on a phantom, the dimensions of the antenna and phantom are taken into account. The diameter of the phantom is 96 mm. The center frequency of 3.11 GHz is considered and the wavelength corresponding to it is calculated, which is 96.36 mm. The length of the horn antenna is 68 mm and the operating frequency of interest considered is 3.11 GHz, so the far-field range of the horn antenna is estimated to be any distance greater than half of 84 mm. The overall dimension of the antenna and phantom together is greater than half the wavelength. The radiative near field is estimated to be in the range of 20 mm to 42 mm. The power transfer efficiency of the antenna is estimated for near-field distances between the proposed antenna and reference horn antenna, which are 0.21λ, 0.31 λ, and 0.41 λ respectively. The far-field region is estimated to be any distance greater than 42 mm.

$$0.62 \times \sqrt{\frac{D^3}{\lambda}} \leq \text{RNF} \leq \frac{2D^2}{\lambda} \tag{1}$$

$$\frac{2D^2}{\lambda} < \text{FF} \tag{2}$$

The S_{21} can be calculated as shown in (3). Where the output power is the power received at the receiver side and the input power is the power transmitted by the transmitter antenna.

$$S_{21} = 10 \times \log(\frac{Outputpower}{Inputpower}) \tag{3}$$

The power transfer efficiency (PTE) can be represented in terms of S_{21} as shown in (4). While we recognize that Eq. 4 defines the power transfer efficiency (PTE) in a manner that extends beyond the proposed antenna alone. To clarify, the PTE formula utilized offers a comprehensive assessment of power transfer between the proposed antenna and the receiving system. Although the measured S21 parameter, defined

This article has been accepted for publication in IEEE Open Journal of Antennas and Propagation. This is the author's version which has not been fully edited and content may change prior to final publication. Citation information: DOI 10.1109/OJAP.2024.3520069

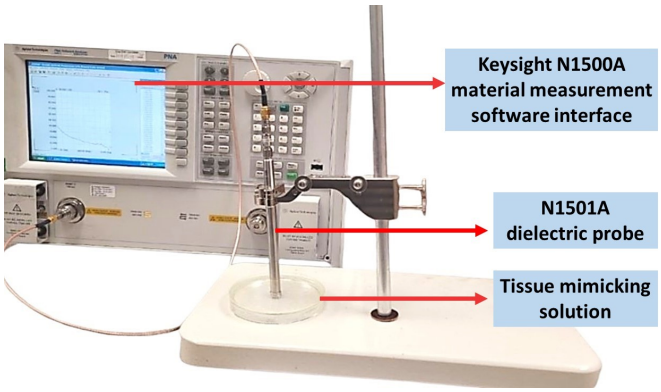

FIGURE 3. Relative permittivity measurement setup of the tissue mimicking solution.

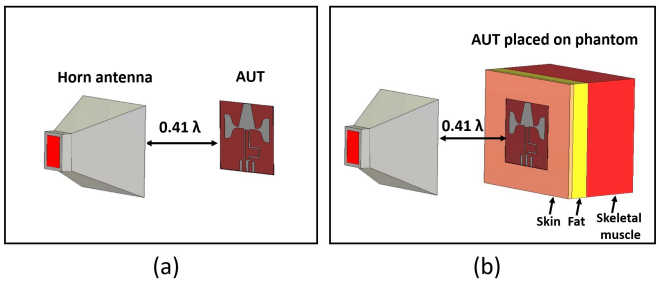

FIGURE 4. Simulation setup for extraction of S_{21} parameters (a) antenna in air (b) antenna placed on phantom.

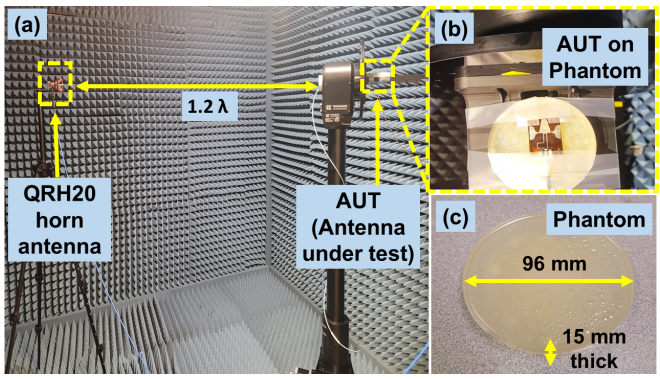

FIGURE 5. Farfield measurement (a) setup in an anechoic chamber (b) antenna on phantom (c) phantom with dimensions.

as the scattering parameter representing power transmission from the proposed to the receiving antenna, includes contributions from both antennas, our methodology normalizes these measured values to focus on the performance of the proposed antenna. Specifically, Eq. 4 is formulated to reflect the PTE relative to the proposed antenna's characteristics, while accounting for the influence of the receiving antenna. This approach ensures that the calculated efficiency accurately represents the proposed antenna's performance within its operational context. We provide a detailed analysis and comparison to show that the performance metrics derived from S_{21} are correctly interpreted and relevant to the proposed design's evaluation. Additionally, we discuss how the formula integrates with our experimental setup to isolate and emphasize the proposed antenna's performance, thereby addressing concerns related to the receiving antenna's gain and efficiency. The percentage of PTE is calculated using (4) with measured S_{21} values.

$$PTE(\%) = 10^{\frac{|S_{21}|}{10}} \times 100\% \tag{4}$$

The tissue mimicking solution's dielectric properties are measured utilizing the N1500A Keysight's Material Measurement Suite, which is connected with Keysight's E8361C PNA Microwave Network Analyzer and N1500A dielectric probe kit as shown in Fig. 3. The S_{21} parameters are simulated by placing the aforementioned transmitter antenna (horn antenna) and the receiver antenna (UWB antenna) in the near-field region as shown in the Fig. 4. The far-field measurement setup for S_{21} measurements is presented in Fig. 5. The horn antenna utilized has an operational bandwidth from 2 to 40 GHz with a gain ranging from 8 to 16 dBi within the operational bandwidth. The gain of horn at the center frequency of the UWB antenna is observed as 7.5 dBi. The feed port of the horn antenna is 50Ω matched. The beam width of the horn antenna at 3.11 GHz is noted as 65° with cross-port isolation of -35 dB.

V. Results and Discussion

A. S-parameter results

The step-wise design evolution of the antenna design is considered and the corresponding S_{11} parameters are presented in Fig. 6. The step-1 result portrayed the narrow operational bandwidth, the step-2 in which a loop strip is incorporated into the feed line has shown in bandwidth improvement and the final step resulted in -55 dB magnitude at the resonating frequency. The fractional bandwidth (F_b) can be calculated using the (5). The S-parameter performance results of considered bend test scenarios as a part of material deformation analysis are presented in Fig. 7. It is observed that the resonant frequency of S_{11} parameter shifted slightly towards the right due to material deformation. It is to be noted that the antenna is still working within the operational bandwidth and has less bandwidth in the bent cases when compared to the non-bent case. It is observed that in the case of the antenna in air, there is less loss when compared to the case where the antenna is tested on the phantom. This shows that the dielectric properties of the phantom would affect the overall antenna's performance when in contact. The measured and simulated S_{11} parameters for the aforementioned two case scenarios are presented in Fig. 8. The realized bandwidth with placing an antenna on the phantom is 2.43 GHz (fractional bandwidth (FBW) of 60.52%) with the achieved magnitude value of -25.17 dB at 3.11 GHz. The measured bandwidth without placing the

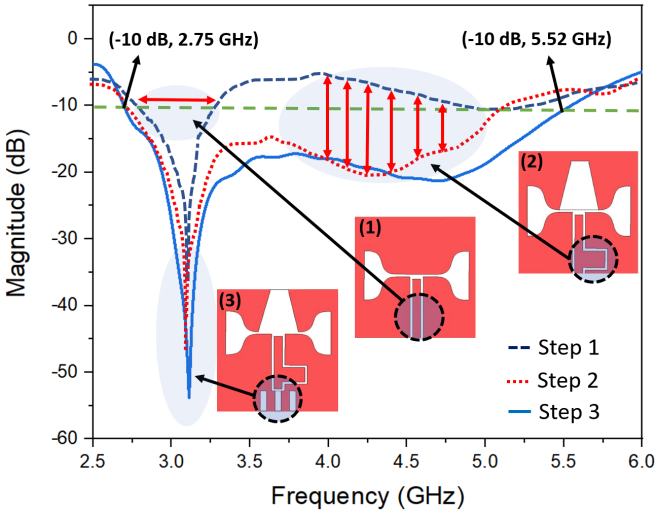

FIGURE 6. Simulated S_{11} parameters for design evolution steps of the antenna.

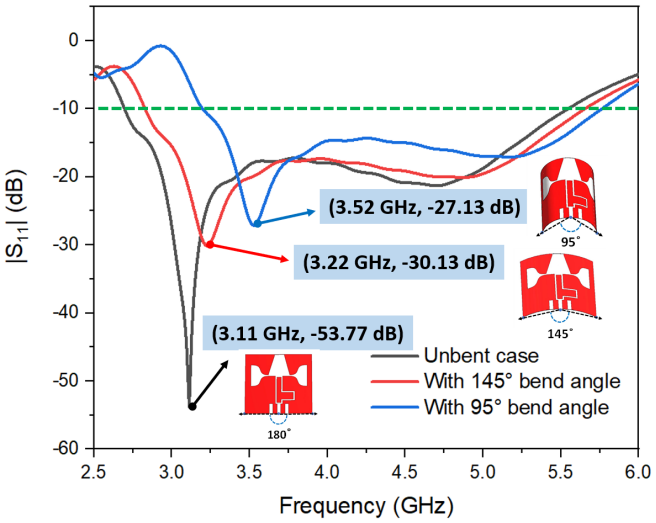

FIGURE 7. $|S_{11}|$ results of considered bend test scenarios for material deformation analysis.

antenna on the phantom is 2.85 GHz (FBW of 69.93%). The better resonance of the UWB antenna at 3.11 GHz is observed for the cases with no phantom involved. This is due to the fact that the dielectric properties would change for the scenario of antenna placement on the fabricated human tissue phantom. As shown in Fig. 9, the S_{21} values were analyzed for the estimated near-field distances, 0.21λ, 0.31 λ, and 0.41 λ are -3.90 dB, -4.67 dB, and -6.55 dB, respectively, with PTE of 66.3 percent, 58.4 and 47.1 percent correspondingly. The measured and simulated S_{21} parameters for the antenna in air and on phantom scenarios are presented in Fig. 11. The slight deviation of the simulation results with respect to measured results is due to the fact that the simulation process does not account for losses associated with the SMA connector.

$$F_b = \frac{f_{\omega_H} - f_{\omega_L}}{f_c} \tag{5}$$

$$f_c = \frac{f_{\omega_H} + f_{\omega_L}}{2} \tag{6}$$

where f_{ω_H} is the upper frequency bound, f_{ω_L} is the lower frequency bound, and f_c is the center frequency which is the arithmetic mean of lowest and upper frequency bound and can be calculated using (6).

B. Discussion on far-field and near-field performances

The maximum and minimum S_{21} values for near-field measurements are presented in Table III. The near-field distance (d_n) is varied within the near-field region to analyze the path loss, at 0.20 λ the maximum of -3.90 dB and a minimum of -6.76 dB is observed, whereas at 0.31 λ, a maximum of -4.67 dB and a minimum of -9.65 dB is observed, and at 0.41 λ the maximum of -6.55 dB and a minimum of -11.43 dB is observed. These results were in agreement with theoretical expectations that the value of S_{21} should attenuate

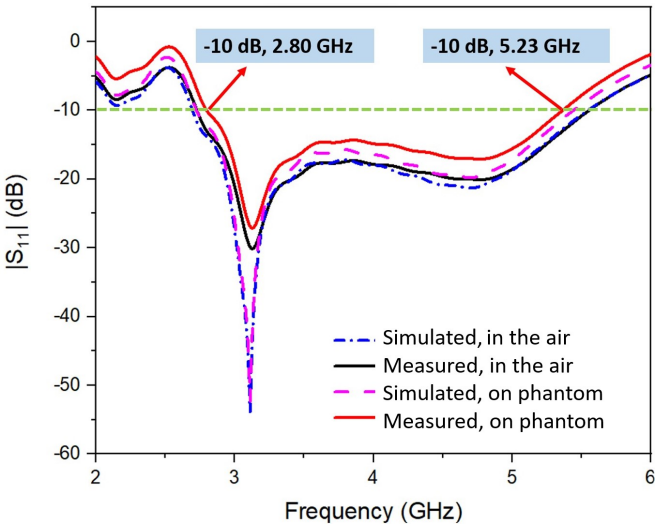

FIGURE 8. Measured and simulated S_{11} parameter for antenna in air and on the phantom.

as the distance of operation increases, and vice-versa. The far-field measured maximum and minimum S_{21} values are presented in Table IV. The antenna in-air case has measured a maximum S_{21} value of -10.09 dB and a minimum of -22.04 dB, whereas the antenna on the phantom case measured a maximum S_{21} value of -19.41 dB and a minimum of -30.58 dB. The measured and simulated S_{21} parameters for the antenna in air and on phantom scenarios are presented in Fig. 11. The slight deviation of the simulation results with respect to measured results is due to the fact that the simulation process does not account for losses associated with the SMA connector.

The graphical visualization of the near-field measurement setup is presented in Fig. 12. The dielectric measurement with permittivity and loss tangent results are portrayed in

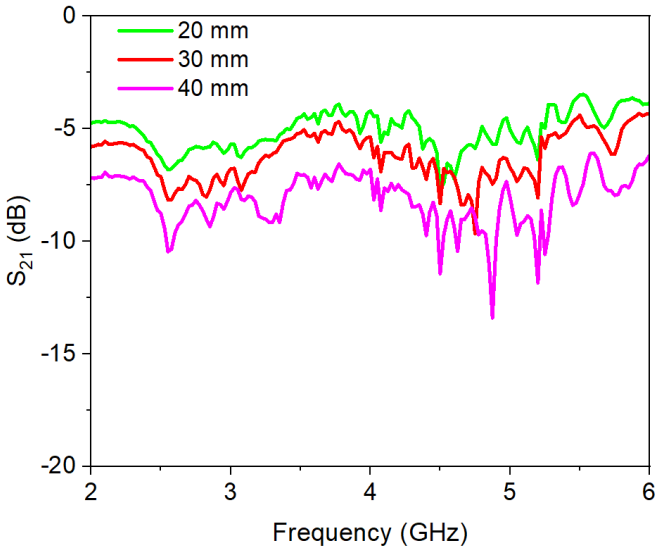

FIGURE 9. Measured S_{21} parameters in near-field region.

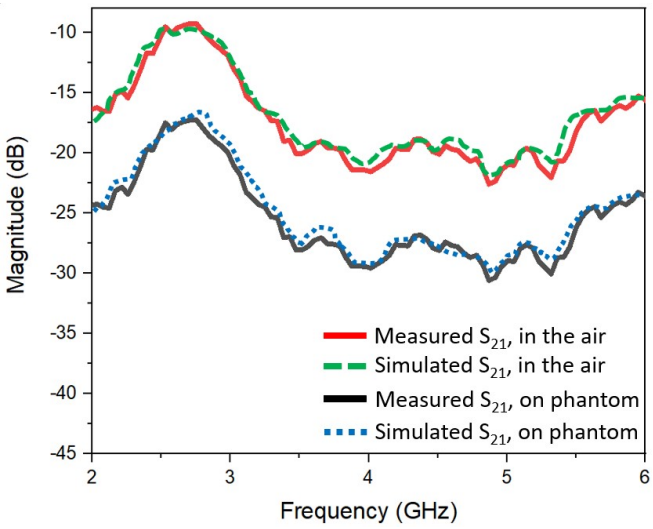

FIGURE 11. Measured and simulated S_{21} parameters for in air and on phantom cases.

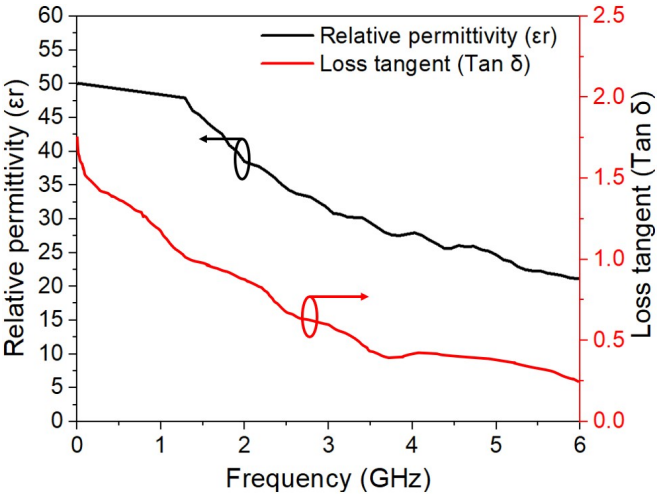

FIGURE 10. Measured relative permittivity and loss tangent plots of the tissue-mimicking solution.

Fig. 11 shows the dielectric constant of the prepared tissue mimicking solution as 30.6 at 3.11 GHz frequency, which is near to the average dielectric constant value (≈32) of the three human tissue layers considered. The simulated results were in good match with the measured results as the permittivity of the fabricated phantom is nearly the same as the average permittivity of the 3 layers considered in the phantom design. Also, the distance between the transmitter and receiver is considered the same for both simulated and measured cases.

C. Comparision on far-field and near-field performances

The comparison between the far-field and nearfield results aligns with theoretical expectations, indicating that as the distance of operation increases, the S_{21} value attenuates, resulting in a higher loss. Comparing the near-field and far-field measurements, it can be observed that the far-field S_{21} values demonstrate significantly higher attenuation. For instance, the maximum S_{21} in the nearfield is -6.55 dB, whereas in the farfield on the phantom case, it is -19.41 dB, indicating approximately 2.96 times higher attenuation in the farfield. Similarly, the minimum S_{21} in the nearfield is -11.43 dB, whereas in the farfield on the phantom case, it is -30.58 dB, representing approximately 2.68 times higher attenuation in the farfield. The comparison reveals that the far-field performance of the UWB antenna shows considerably higher levels of attenuation compared to the near-field performance.

D. PTE variation for antenna in air and on phantom

The S_{21} parameters were measured for two case scenarios which are antenna in air and when placed on fabricated human tissue phantom. The far-field measured S_{21} values for the case where the UWB antenna is placed on a human tissue phantom is -23.17 dB with a corresponding far-field PTE value of 0.48 %. In the case where the antenna is moved from human phantom to air, measured S_{21} value is -15.20 dB, with a far-field PTE value of 3.02 %. Fig. 10 presents the measured relative permittivity and loss tangent plots of the tissue-mimicking solution. The observed variation in S21 values arises from the distinct conditions under which the simulations were conducted. Fig. 11 shows the overall S21 performance of the antenna in free space and on the phantom. The presence of the lossy phantom material causes a significant reduction of approximately 5 dB, attributed to increased near-field energy absorption and surface wave propagation. Although the Friis free space formula accounts for far-field transmission losses based on gain differences, it does not fully capture the near-field interactions and absorption effects introduced by the phantom, especially when close to the antenna. As a result, the larger S21 difference is due to cumulative near-field losses. These factors explain the

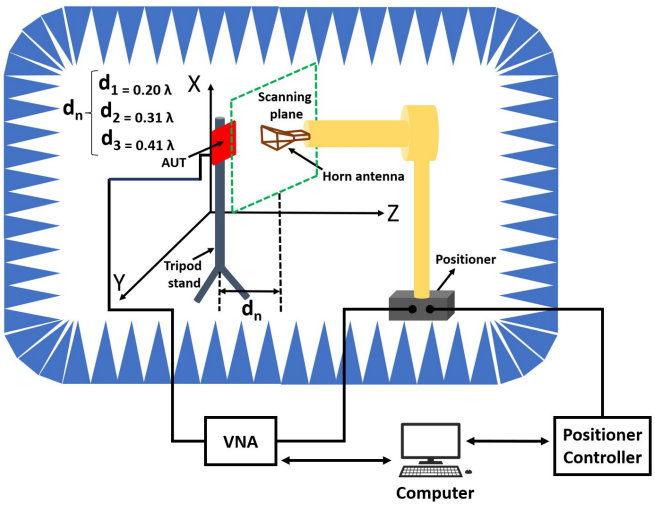

FIGURE 12. Graphical visualization of the near-field measurement setup.

variation in S21 reduction while remaining consistent with electromagnetic theory.

The wireless power transfer (WPT) system analyzed in this study consists the proposed ultra-wideband (UWB) antenna and a broadband horn antenna (QRH20) to comprehensively assess the WPT performance. A full-system investigation revealed a maximum power transfer efficiency (PTE) of 66.3% at a near-field distance of 0.3λ, supported by corresponding transmission coefficients S_{21} of -3.90 dB. These results validate the practicality of the proposed UWB antenna within a meticulously structured WPT framework. While this work primarily emphasize the optimization of a single antenna element, it establishes a robust foundation for future scalability into $N \times N$ antenna arrays. This scalability holds the potential to significantly enhance system-level performance, paving the way for innovations in high-efficiency WPT applications. This initial effort marks a pivotal step toward addressing the complexities of large-scale WPT systems, providing critical insights for future investigations into the scalability, efficiency, and dynamic adaptability of UWB-based antenna arrays.

E. Gain variation for antenna in air and on phantom

The gain versus theta plots for the aforementioned two case scenarios of the antenna in air, and on human tissue phantom were presented in Fig. 13. The cases involved in the phantom had comparably lower gain values when compared to cases where there is no phantom involved. This is due to the fact that the human phantom partially absorbs the radiation emitted out of the antenna placed on the phantom. Similarly, the maximum gain versus over the frequency of 2 GHz to 6 GHz is presented in Fig. 13. The simulated and measured gain values were in good agreement with each other.

The measured co-polarization and cross-polarization plots with amplitude and phase data corresponding to -25 inch to 25 inch scanning plane with respective proposed antenna are presented in Fig. 14.

TABLE 3. Maximum and minimum S_{21} for near-field measurements at measured frequency of 3.11 GHz

Near-field distance (d_n)	Max. value (dB)	Min. value (dB)
0.20 λ	-3.90	-6.76
0.31 λ	-4.67	-9.65
0.41 λ	-6.55	-11.43

* d_n is the distance considered between AUT and the reference antenna.

TABLE 4. Maximum and minimum S_{21} for far-field measurements at measured frequency of 3.11 GHz

Antenna case	Far-field distance (d_f)	Max. value (dB)	Min. value (dB)
In air	1.2 λ	-10.09	-22.04
On phantom	1.2 λ	-19.41	-30.58

It can be observed in Fig. 14 (b), that the transmitted power is concentrated within -10 inch to 10 inch near-field scanning plane area, which indicates its good power transmission efficiency. The performance comparison of this work with similar prior studies is presented in Table V. Fig. 15 presents the measured and simulated cartesian-gain plots for in-air and on-phantom cases. The simulated gain plots for each design evolution step are presented in Fig. 16 which portray nearly 3 dBi of maximum gain enhancement from the initial to the final step of the evolution stages. The 3D radiation patterns for the proposed antenna are presented in Fig. 17(a) and the antenna with body model is presented in Fig. 17(b). The antenna alone has portrayed a high gain of 6.89 dBi and with the body model, the gain is observed to be 5.46 dBi. It is observed that there is a 1.43 dBi of gain variation due to the presence of the body model. The

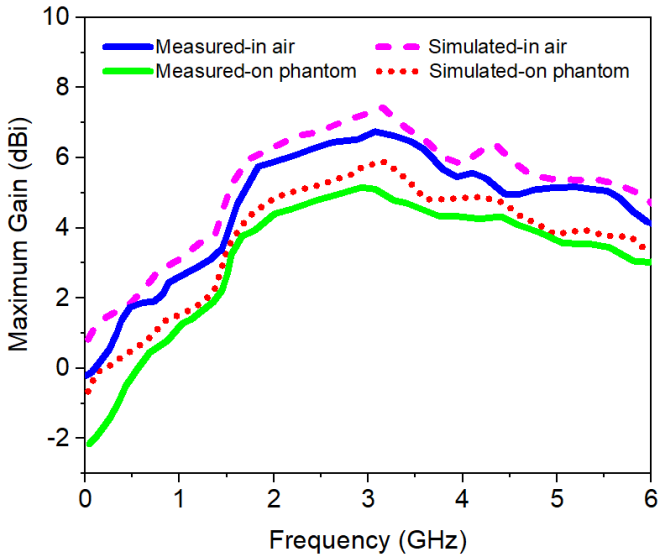

FIGURE 13. Maximum gain versus frequency for 2 cases: the antenna in air, and the antenna on a phantom.

This article has been accepted for publication in IEEE Open Journal of Antennas and Propagation. This is the author's version which has not been fully edited and content may change prior to final publication. Citation information: DOI 10.1109/OJAP.2024.3520069

TABLE 5. Comparison with state of the art works

Reference	Dimension (mm^2)	Resonating frequency (GHz)	Max. Gain (dBi)	Max. Fractional-Bandwidth (%)	PTE (%)
[12]	80×67	3.10	4.53	94.28	45
[13]	20×25	3.11	5.25	91.33	92
[14]	27.5×19.5	2.45	4.5	60	27
[37]	41×41	2.45	3.75	45	91.4
[38]	20×26	3.6	3.86	13.6	NA
[39]	70×40	3.11	8.50	40	95
This Work	30×33.7	3.11	6.35	69.93	66.3

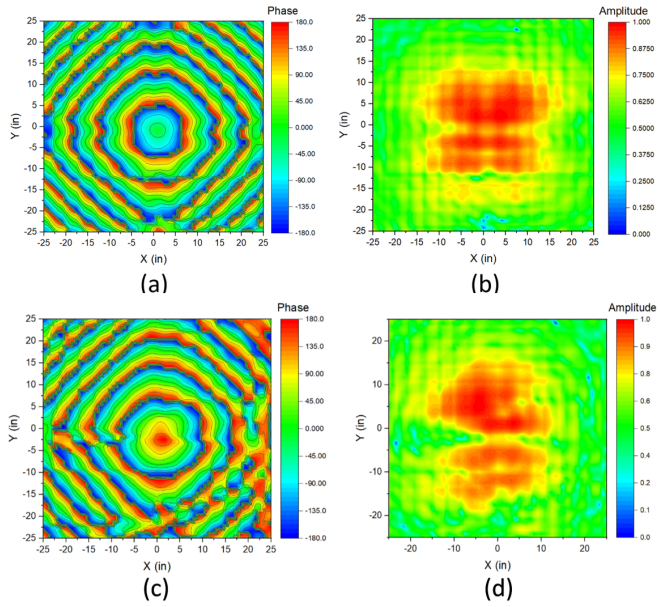

FIGURE 14. Measured Co-pol and Cross-pol data at 3.11 GHz, (a) Co-polarization Phase (b) Co-polarization Amplitude, (c) Cross-polarization Phase (d) Cross-polarization Magnitude.

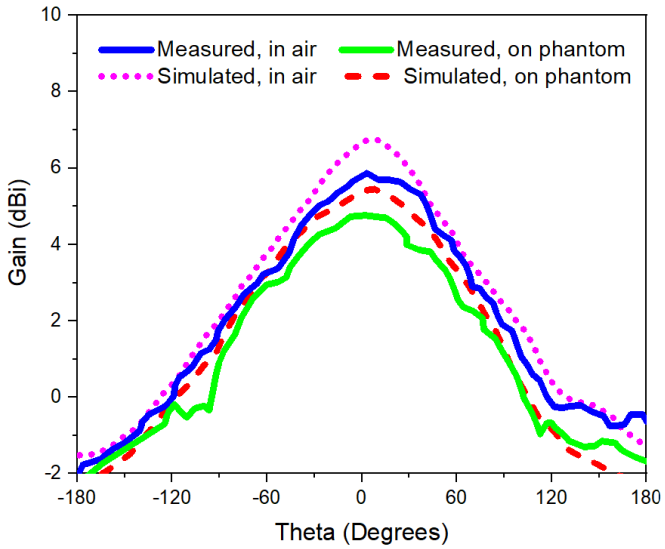

FIGURE 15. Measured and Simulated gain versus theta for the in-air and on-phantom cases at 3.11 GHz resonant frequency.

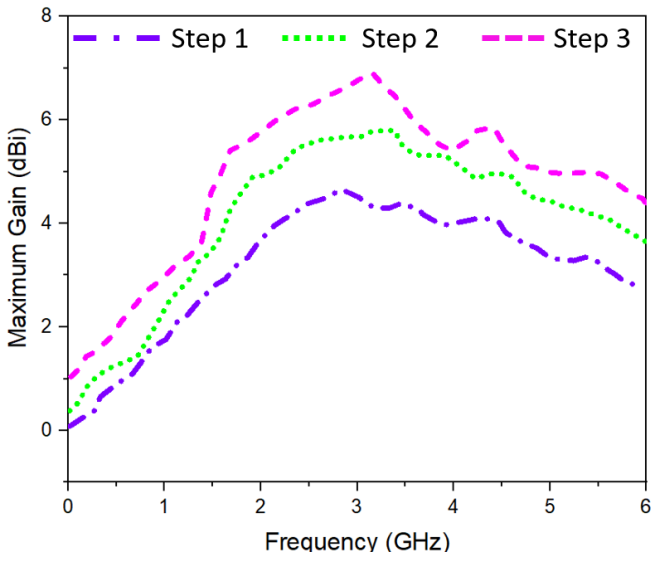

FIGURE 16. Simulated maximum gain versus frequency for antenna design evolution steps.

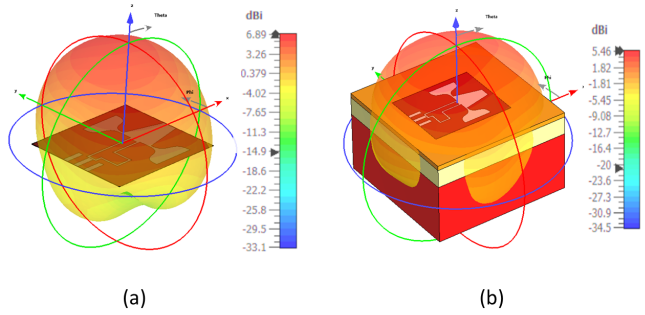

FIGURE 17. 3D radiation patterns (a) designed antenna and (b) antenna with body model.

normalized polar plots with measured and simulated co-pol and cross-pol patterns at 3.11 GHz, 4 GHz, and 5 GHz are presented in Fig. 18. Both the measured and simulated data were observed to be in good correlation with each other. The close alignment between the measured and simulated results underscores the accuracy of the measurements and

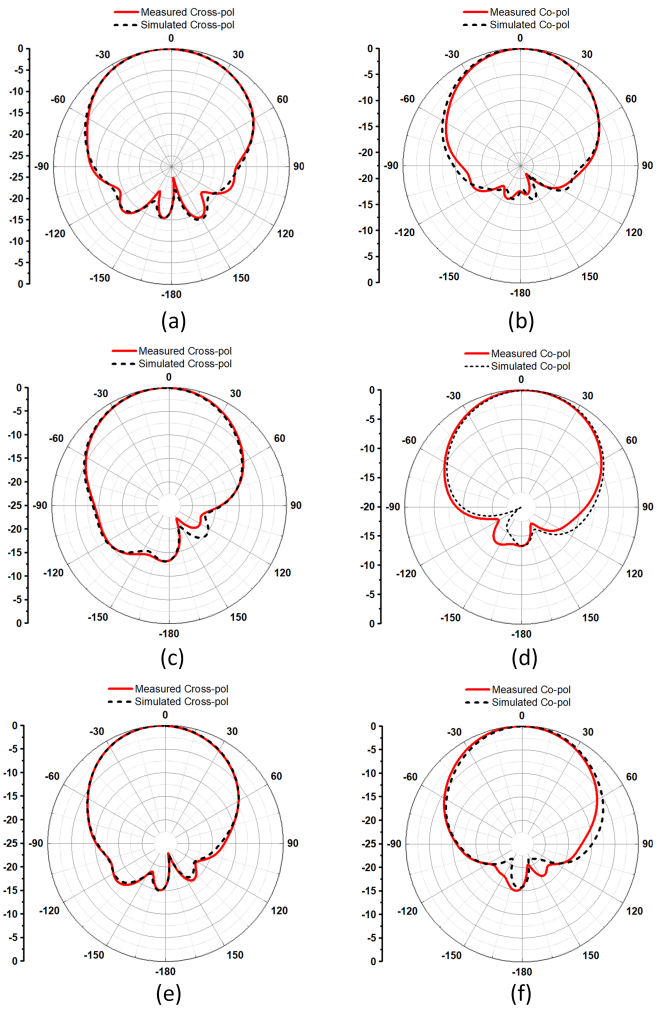

FIGURE 18. **Normalized 2D polar plots at 3.11 GHz, 4 GHz, and 5 GHz (a) Cross-pol at 3.11 GHz, (b) Co-pol at 3.11 GHz, (c) Cross-pol at 4 GHz, (d) Co-pol at 4 GHz, (e) Cross-pol at 5 GHz, (f) Co-pol at 5 GHz.**

the reliability of the simulation in depicting the antenna's radiation characteristics.

The SAR analysis is carried out for the operational bandwidth for SAR averaged over 1 g and 10 g of human skeletal tissue respectively. The safe SAR limits as suggested by ICNIRP (International Commission on Non-Ionizing Radiation Protection) are 1.6 W/kg averaged over 1 g of human tissue and 2 W/kg when averaged over 10 g of human tissue respectively [40]. The maximum SAR value observed is 0.794 W/kg and 1.02 W/kg when averaged over 10 g tissue and 1 g tissue respectively. Fig. 19(a) presents the simulated SAR averaged over 10 g and Fig. 19(b) presents SAR averaged over 1 g. The SAR simulated values over the frequency band are presented in Fig. 20. The SAR values analyzed over the operational bandwidth for an input power of 10 dBm were within the safe limits.

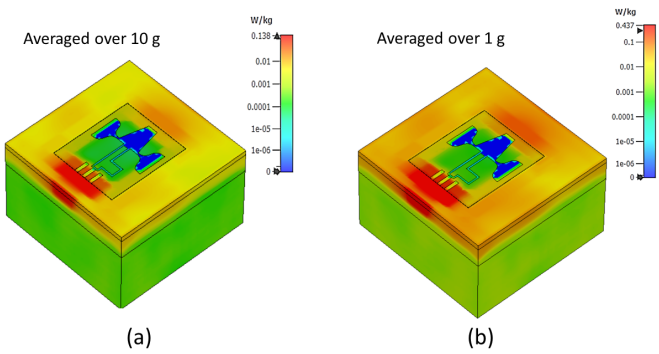

FIGURE 19. **SAR simulated results at 3.11 GHz.**

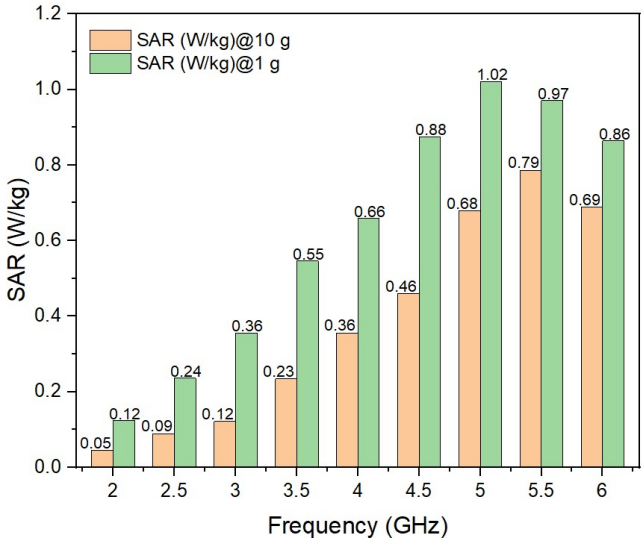

FIGURE 20. **Simulated SAR over the frequency band.**

VI. Conclusion

This work presented a high-gain compact UWB antenna for wireless power transfer applications. The proposed antenna is highly suitable for WPT applications due to its UWB performance, compact size, and high gain characteristics. The antenna achieves a fractional bandwidth (FBW) of 69.93%, enabling efficient operation across a wide frequency range, which is critical for optimizing power transfer efficiency (PTE) across different bands. Unlike conventional microstrip patch and bowtie antennas, which are often constrained by limited bandwidth or large physical dimensions, the proposed design incorporates a loop strip within the feed structure to improve impedance matching and suppress anti-phase currents. This results in enhanced bandwidth and gain without compromising the compact form factor, making the antenna ideal for space-constrained WPT applications. Additionally, the antenna's SAR analysis ensures safety in wearable scenarios, further enhancing its suitability for WPT on human tissue phantoms. The power transfer efficiency of the antenna in air and when placed on the phantom is analyzed and compared with simulated results. Additionally,

both near-field and far-field S_{21} parameters were analyzed. The simulated SAR values were within the safe limits as suggested by ICNIRP, which indicates that it is safe to wear on the human body. The proposed antenna has its measured results in alignment with the simulation results and portrays the best performance capability and suitability for wearable WPT applications. In conclusion, the designed UWB antenna has demonstrated a gain of 6.35 dBi along with a fractional bandwidth (FBW) of 69.93%. The nearfield S_{21} parameter exhibited a maximum power transfer efficiency (PTE) of 66.3% at a distance of 0.3λ. Additionally, the estimated specific absorption rate (SAR) values of 0.794 W/kg for a 10 g tissue average and 1.02 W/kg for a 1 g tissue average affirm the safety and suitability of the proposed design and its potential for advancing wearable WPT applications.

Acknowledgment

This study is supported by the National Science Foundation (NSF) with the grant number ECCS 2246559.

REFERENCES

[1] H. Zhang, N. Shlezinger, F. Guidi, D. Dardari, M. F. Imani, and Y. C. Eldar, "Near-field wireless power transfer with dynamic metasurface antennas," *arXiv preprint arXiv:2110.04885*, 2021.

[2] N. Shinohara, "History and innovation of wireless power transfer via microwaves," *IEEE Journal of Microwaves*, vol. 1, no. 1, pp. 218–228, 2021.

[3] J. Barreto, G. Perez, A.-S. Kaddour, and S. V. Georgakopoulos, "A study of wearable wireless power transfer systems on the human body," *IEEE Open Journal of Antennas and Propagation*, vol. 2, pp. 86–94, 2021.

[4] H. Cheng and H. Zhang, "Investigation of improved methods in power transfer efficiency for radiating near-field wireless power transfer," *Journal of Electrical and Computer Engineering*, vol. 2016, 2016.

[5] K. Kakaraparty and I. Mahbub, "The design and sar analysis of wearable uwb antenna for radiative near-field wireless power transfer," in *2022 IEEE MTT-S International Microwave Biomedical Conference (IMBioC)*. IEEE, 2022, pp. 141–143.

[6] A. Iqbal, M. Al-Hasan, I. B. Mabrouk, A. Basir, M. Nedil, and H. Yoo, "Biotelemetry and wireless powering of biomedical implants using a rectifier integrated self-diplexing implantable antenna," *IEEE Transactions on Microwave Theory and Techniques*, vol. 69, no. 7, pp. 3438–3451, 2021.

[7] J. Zhang, R. Das, J. Zhao, N. Mirzai, J. Mercer, and H. Heidari, "Battery-free and wireless technologies for cardiovascular implantable medical devices," *Advanced Materials Technologies*, vol. 7, no. 6, p. 2101086, 2022.

[8] L. Ukkonen, L. Sydänheimo, T. Björninen, and S. Ma, "Antennas and wireless power transfer for brain-implantable sensors," *Antenna and Sensor Technologies in Modern Medical Applications*, pp. 91–143, 2021.

[9] X. Yang, W. Geyi, and H. Sun, "Optimum design of wireless power transmission system using microstrip patch antenna arrays," *IEEE Antennas and Wireless Propagation Letters*, vol. 16, pp. 1824–1827, 2017.

[10] B. Maity and S. K. Nayak, "A high gain narrowband microstrip antenna array for wireless applications," in *2021 International Symposium on Antennas and Propagation (ISAP)*. IEEE, 2021, pp. 1–2.

[11] K. Kakaraparty and I. Mahbub, "The design and sar analysis of a uwb bow-tie antenna for wireless wearable sensors," in *2022 United States National Committee of URSI National Radio Science Meeting (USNC-URSI NRSM)*. IEEE, 2022, pp. 204–205.

[12] R. B. V. B. Simorangkir, A. Kiourti, and K. P. Esselle, "Uwb wearable antenna with a full ground plane based on pdms-embedded conductive fabric," *IEEE Antennas and Wireless Propagation Letters*, vol. 17, no. 3, pp. 493–496, 2018.

[13] P. Sambandam, M. Kanagasabai, S. Ramadoss, R. Natarajan, M. G. N. Alsath, S. Shanmuganathan, M. Sindhadevi, and S. K. Palaniswamy, "Compact monopole antenna backed with fork-slotted ebg for wearable applications," *IEEE Antennas and Wireless Propagation Letters*, vol. 19, no. 2, pp. 228–232, 2020.

[14] B. J. DeLong, A. Kiourti, and J. L. Volakis, "A radiating near-field patch rectenna for wireless power transfer to medical implants at 2.4 ghz," *IEEE Journal of Electromagnetics, RF and Microwaves in Medicine and Biology*, vol. 2, no. 1, pp. 64–69, 2018.

[15] K. Kakaraparty and I. Mahbub, "Smart-watch integrated flexible strap antenna for enhanced wifi and bluetooth connectivity applications," in *2024 IEEE International Symposium on Antennas and Propagation and INC/USNC-URSI Radio Science Meeting (AP-S/INC-USNC-URSI)*, 2024, pp. 871–872.

[16] M. Wang, H. Liu, P. Zhang, X. Zhang, H. Yang, G. Zhou, and L. Li, "Broadband implantable antenna for wireless power transfer in cardiac pacemaker applications," *IEEE Journal of Electromagnetics, RF and Microwaves in Medicine and Biology*, vol. 5, no. 1, pp. 2–8, 2021.

[17] S. Roy, K. Kakaraparty, and I. Mahbub, "Design of a 4x4 ultrawideb and phased array antenna for wireless power transfer application," in *2022 IEEE International Symposium on Antennas and Propagation and USNC-URSI Radio Science Meeting (AP-S/URSI)*, 2022, pp. 1296–1297.

[18] K. Kakaraparty and I. Mahbub, "Design and sar analysis of a meander slot antenna for backscattering rfid applications," in *2023 United States National Committee of URSI National Radio Science Meeting (USNC-URSI NRSM)*, 2023, pp. 141–142.

[19] W. Zhou, P. Wu, W. C. Mu, W. Yu, and S. Y. Huang, "Compact broadband planar resonator with a viaed double spiral for robust wireless power transfer," *IEEE Journal of Electromagnetics, RF and Microwaves in Medicine and Biology*, vol. 5, no. 4, pp. 329–339, 2021.

[20] A. I. Hammoodi and J. K. Ali, "Practical bending studying on uwb pentagonal flexible antenna," in *2020 IEEE International Symposium on Antennas and Propagation and North American Radio Science Meeting*, 2020, pp. 413–414.

[21] M. Kanagasabai, P. Sambandam, M. G. N. Alsath, S. Palaniswamy, A. Ravichandran, and C. Girinathan, "Miniaturized circularly polarized uwb antenna for body centric communication," *IEEE Transactions on Antennas and Propagation*, vol. 70, no. 1, pp. 189–196, 2022.

[22] S. Gayen, B. Biswas, and A. Karmakar, "The quest for a miniaturized antenna in the wireless capsule endoscopy application: a review," *International Journal of Microwave and Wireless Technologies*, pp. 1–11, 2021.

[23] M. Sharma, Y. Awasthi, H. Singh, R. Kumar, and S. Kumari, "Compact printed high rejection triple band-notch uwb antenna with multiple wireless applications," *Engineering science and technology, an international journal*, vol. 19, no. 3, pp. 1626–1634, 2016.

[24] G. Fadehan, K. B. Adedeji, and Y. O. Olasoji, "Parametric study and analysis of modified electromagnetic band gap in frequency notching of ultra-wide band antenna," in *International Journal of Engineering Research in Africa*, vol. 61. Trans Tech Publ, 2022, pp. 151–164.

[25] M. Wagih, A. Komolafe, A. S. Weddell, and S. Beeby, "Broadband compact substrate-independent textile wearable antenna for simultaneous near-and far-field wireless power transmission," *IEEE Open Journal of Antennas and Propagation*, vol. 3, pp. 398–411, 2022.

[26] S. Roy, K. Kakaraparty, and I. Mahbub, "A slot-connected cavity design with corresponding equivalent circuit model analysis for fully metallic 3-d vivaldi antenna for wireless power telemetry applications," *IEEE Open Journal of Antennas and Propagation*, vol. 5, no. 1, pp. 130–139, 2024.

[27] L. A. Y. Poffelie, P. J. Soh, S. Yan, and G. A. Vandenbosch, "A high-fidelity all-textile uwb antenna with low back radiation for off-body wban applications," *IEEE Transactions on antennas and propagation*, vol. 64, no. 2, pp. 757–760, 2015.

[28] P. B. Samal, S. J. Chen, and C. Fumeaux, "Wearable textile multiband antenna for wban applications," *IEEE Transactions on Antennas and Propagation*, vol. 71, no. 2, pp. 1391–1402, 2022.

[29] Z. Chen, X. Zheng, C. Song, J. Zhang, V. Volskiy, Y. Li, and G. A. Vandenbosch, "Enhancing circular polarization performance of low-profile patch antennas for wearables using characteristic mode analysis," *Sensors*, vol. 23, no. 5, p. 2474, 2023.

[30] M. Fernández, C. Vázquez, and S. Ver Hoeye, "2.4 ghz fully woven textile-integrated circularly polarized rectenna for wireless power transfer applications," *IEEE Access*, vol. 12, pp. 89 836–89 844, 2024.

[31] R. Gopika, C. Saha, and Y. M. M. Antar, "A novel yagi element integrated nested loop quasi-self-complementary dual-port combiner radiator," *IEEE Open Journal of Antennas and Propagation*, vol. 5, no. 2, pp. 487–494, 2024.
[32] X. Yang, E. L. Bennett, I. Calisir, Q. Hua, J. Xiao, and Y. Huang, "A study of wideband dielectric resonator antennas loaded with special dispersive materials," *IEEE Open Journal of Antennas and Propagation*, vol. 5, no. 6, pp. 1658–1670, 2024.
[33] Y. Ma, C. Liu, Y. Huang, H. Ke, and X. Liu, "Combined magneto-electric/coil receiving antenna for biomedical wireless power transfer," *IEEE Journal of Electromagnetics, RF and Microwaves in Medicine and Biology*, pp. 1–12, 2024.
[34] A. Alemaryeen and S. Noghanian, "Electromagnetic and thermal co-analysis of an implanted dipole antenna," *IEEE Open Journal of Antennas and Propagation*, vol. 5, no. 6, pp. 1539–1550, 2024.
[35] "Characterization and evaluation of tissue-mimicking gelatin phantoms, doi: https://www.ncbi.nlm.nih.gov/pmc/articles/pmc4490606/."
[36] S. Di Meo, A. Cannatà, C. Macchello, S. Morganti, M. Pasian, and G. Matrone, "Bi-modal tissue-mimicking breast phantoms: comparison between the performance of agar- and gelatin-based phantoms," in *2022 3rd URSI Atlantic and Asia Pacific Radio Science Meeting (AT-AP-RASC)*, 2022, pp. 1–4.
[37] U. Musa, S. M. Shah, H. A. Majid, I. A. Mahadi, M. K. A. Rahim, M. S. Yahya, and Z. Z. Abidin, "Design and analysis of a compact dual-band wearable antenna for wban applications," *IEEE Access*, vol. 11, pp. 30 996–31 009, 2023.
[38] A. Abbas, N. Hussain, J. Lee, S. G. Park, and N. Kim, "Triple rectangular notch uwb antenna using ebg and srr," *IEEE Access*, vol. 9, pp. 2508–2515, 2021.
[39] J.-Y. Lee, J. Choi, J.-H. Jang, and W. Hong, "Performance enhancement in compact inverted-l antenna by using 1-d ebg ground structures and beam directors," *IEEE Access*, vol. 7, pp. 93 264–93 274, 2019.
[40] I. C. on Non-Ionizing Radiation Protection *et al.*, "Guidelines for limiting exposure to electromagnetic fields (100 khz to 300 ghz)," *Health physics*, vol. 118, no. 5, pp. 483–524, 2020.

Dr. Karthik Kakaraparty (Graduate Member, IEEE) earned his Doctoral degree in Electrical Engineering from the University of Texas at Dallas in the Summer of 2024, where he conducted research under the supervision of Prof. Ifana Mahbub. He received his Master's degree in Electrical Engineering from the University of North Texas in 2021, with a thesis focused on CMOS-based compressive sensing circuits for neural data acquisition and reverse electrowetting energy harvesting for self-powered wearable sensors. His doctoral research centered on the design of compact, high-gain, ultra-wideband millimeter-wave antennas for drone-to-drone communication. His broader research interests include bias-free energy harvesting using high-dielectric flexible electrodes with reverse electrowetting, wearable and flexible antenna design for on-body electronics, efficient wireless data transmission for in-situ soil sensing, and the development of low-cost, ultra-wideband 3D-printed antennas for RADAR applications. Dr. Kakaraparty has petitioned and formed the IEEE APS-MTTS Joint Chapter at UT Dallas and served as Chapter Chair for 2023-2024, and is an active reviewer for IEEE Transactions on Antennas and Propagation, IEEE Transactions on Microwave Theory and Techniques, IEEE Open Journal of Antennas and Propagation, and IEEE Sensors Journal.

Dr. Ifana Mahbub (Senior Member, IEEE) is an Associate Professor and the Texas Instrument's Early Career Chair Awardee in the Department of Electrical and Computer Engineering at the University of Texas at Dallas, where she is leading the Integrated Biomedical, RF Circuits and Systems Laboratory (iBioRFCASL). Her research interests include ultrawideband/mmwave phased-array antenna design for far-field wireless power transfer and vehicle-to-vehicle (V2V) communication. She received a B.Sc. degree (2012) in Electrical and Electronic Engineering from the Bangladesh University of Engineering and Technology and a Ph.D. degree (2017) in Electrical Engineering from the University of Tennessee, Knoxville. Dr. Mahbub is the recipient of the NSF "Early Career Award" (2020), and the DARPA "Young Faculty Award" (2021). She serves as the secretary for the URSI commission K and as a guest editor for the IEEE Open Journal of Antennas and Propagation and MDPI Sensors Journals. Dr. Mahbub has published 2 book chapters, 29 journal publications, and over 89 peer-reviewed conference publications.